TU Delft

Delft University of Technology

Document Version
Final published version

Licence
CC BY

Citation (APA)
Postma, J. I., Yahyaee, A., & Haverkort, J. W. (2026). Membraneless flow-through water electrolysis: The importance of cell geometry. *Energy Conversion and Management: X*, *32*, Article 102272. https://doi.org/10.1016/j.ecmx.2026.102272

Important note
To cite this publication, please use the final published version (if applicable).
Please check the document version above.

Copyright
In case the licence states “Dutch Copyright Act (Article 25fa)”, this publication was made available Green Open Access via the TU Delft Institutional Repository pursuant to Dutch Copyright Act (Article 25fa, the Taverne amendment). This provision does not affect copyright ownership.
Unless copyright is transferred by contract or statute, it remains with the copyright holder.

Sharing and reuse
Other than for strictly personal use, it is not permitted to download, forward or distribute the text or part of it, without the consent of the author(s) and/or copyright holder(s), unless the work is under an open content license such as Creative Commons.

Takedown policy
Please contact us and provide details if you believe this document breaches copyrights.
We will remove access to the work immediately and investigate your claim.

This work is downloaded from Delft University of Technology.

Energy Conversion and Management: X 32 (2026) 102272

Contents lists available at ScienceDirect

Energy Conversion and Management: X

journal homepage: www.sciencedirect.com/journal/energy-conversion-and-management-x

Membraneless flow-through water electrolysis: The importance of cell geometry

J.I. Postma *,[1], A. Yahyaee[1], J.W. Haverkort

Technische Universiteit Delft, Mechanical Engineering, Process & Energy, Leeghwaterstraat 39, Delft 2628 CB, The Netherlands

ARTICLE INFO

Keywords:
Membraneless electrolyser
Perforated plate electrodes
Discharge channel design
Flow uniformity
Critical velocity
Gas crossover

ABSTRACT

Membraneless flow-through water electrolysers keep the generated hydrogen away from oxygen bubbles by forced convection, removing membrane costs while improving energy efficiency. Previously, micrometre holes were used to ensure a homogeneous flow distribution. Here, we strongly reduce flow resistance using electrodes with large holes, while a discharge channel that widens in the direction of the main flow improves flow distribution. At too low liquid velocities, we provide direct in-situ measurements showing that the bubble size between the electrodes increases over time and with height due to coalescence. Counterintuitively, we find that a straight discharge channel requires less liquid flow. Using a combination of multiphase simulations and imaging experiments, we find that the higher velocity through the final downstream holes in a straight discharge channel prevents gas bubbles in the gap. The superficial velocity at which the electrolyte enters the feed channel must be an order of magnitude greater than that of the hydrogen produced at the electrode. The electrolyte velocity through the last holes should be even two orders of magnitude greater, so the gas fraction stays well below 1 percent there. Interestingly, at lower liquid flow rates, computational fluid dynamics predicts that natural electrolyte convection diverts the flow towards the hydrogen-producing electrode. By identifying the local flow requirements, this work helps to balance low pressure drop with effective gas bubble removal in membraneless electrolysers.

1. Introduction

Alkaline water electrolysis (AWE) stands out as the most mature and cost-effective method for large-scale green hydrogen production [1]. State-of-the-art AWE systems typically employ a zero-gap configuration, where porous electrodes are pressed directly against a diaphragm [2,3]. This diaphragm is essential for separating the hydrogen and oxygen gas streams, thereby ensuring product purity and preventing the formation of explosive mixtures [4,5]. Conventional alkaline electrolysers use a separator between the electrodes, historically asbestos, and since its ban, porous ceramic–polymer composites such as Zirfon [6]. However, separators imposes a significant ionic resistance, which leads to ohmic losses and lowers the overall energy efficiency of the system [7,8]. Furthermore, the harsh alkaline environment and elevated operating temperatures can cause membrane degradation over time, compromising the electrolyser's long-term durability and increasing operational costs [6,9,10]. Finally, diaphragms allow significant crossover of dissolved gases via diffusion and electro-osmotic flow, further degrading gas purity and raising safety concerns [11]. Furthermore, the fluorinated ionomers used in PEM and AEM cells are per- and polyfluoroalkyl substances (PFAS), whose persistence and associated health and environmental risks have drawn increasing regulatory scrutiny [12,13], so that periodic separator replacement carries an environmental as well as a maintenance and capital cost penalty.

To overcome these limitations, several types of membraneless electrolysers are studied as an alternative architecture [14]. By removing the diaphragm, these systems often rely on the convective flow of the electrolyte to separate the product gases. The flow may be parallel to the electrodes in a flow-by configuration or normal to the porous electrodes in a flow-through configuration. The use of flow-through electrodes has a long history with applications including flow batteries, electrosynthesis, and metal removal [15–19]. Application to water electrolysis was studied, e.g., in Refs. [20–22] and more recently for membraneless electrolysis in Refs. [23–32]. This reduces material costs, enhances mass transport, and has the potential to improve energy efficiency by reducing the inter-electrode ionic resistance. However, the performance of membraneless electrolysers critically depends on the management of gas bubbles generated at the electrodes. The formation

* Corresponding author.
E-mail address: j.i.postma-1@tudelft.nl (J.I. Postma).
[1] JI Postma and A Yahyaee are co-first authors.

https://doi.org/10.1016/j.ecmx.2026.102272
Received 31 August 2026; Accepted 1 September 2026
Available online 10 September 2026
2590-1745/© 2026 The Authors. Published by Elsevier Ltd. This is an open access article under the CC BY license (http://creativecommons.org/licenses/by/4.0/).

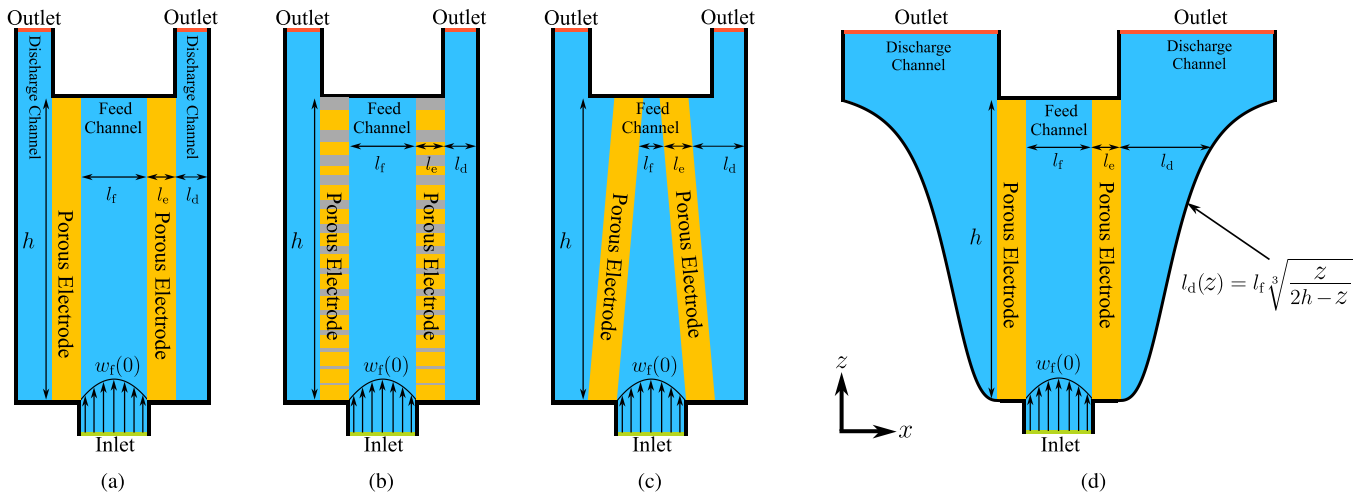


Fig. 1. (a) Schematic of the flow-through electrolyser with (a) straight channels satisfying $l_d = \frac{1}{2} l_f$. (b) an alternative design with a variable-electrode permeability, (c) an alternative with a variable-feed channel width =, and (d) Schematic of the flow-through electrolyser, a variable-width discharge channel designed to promote uniform flow through the electrodes. The discharge channel width $l_d(z)$ varies according to the shown Eq. (1), derived in Appendix A.

and accumulation of bubbles can increase local electrolyte resistance, cause non-uniform current distribution, and take away some electrode area, leading to significant efficiency losses through bubble overpotentials, particularly at high, commercially relevant current densities [33–37]. In areas of low flow velocity, bubbles can become trapped within the electrode's porous structure, exacerbating these issues [35]. A more homogeneous flow distribution seems desirable as it holds the promise of lowering the required inlet velocity. This has the advantage of increasing the outlet gas fraction and thereby lowering the cost of gas-liquid separation.

A key challenge, therefore, is to ensure a uniform electrolyte flow distribution through the electrodes to effectively mitigate bubble accumulation [23]. Previous studies have addressed this by adding an inactive layer [25,26], asymmetrically coating electrodes [27], or using electrodes with a low hydraulic permeability [25]. A high pressure drop across the electrode, relative to the gap height, ensures that the flow is well distributed. However, this increased hydraulic resistance necessitates higher pumping power, suggesting that improvements are possible. Gas separation is achieved by the convective flow itself: the electrolyte enters the central channel vertically and is forced horizontally through the porous electrodes. The H_2 evolved at the cathode moves with the electrolyte into a catholyte discharge channel, and the O_2 evolved at the anode into the anode discharge channel. We note that the product-gas purity of the present cell was not measured. For the closely related divergent electrode-flow-through concept, Gillespie et al. reported 99.8 % H_2 purity [24]. This work introduces a novel approach to address the flow uniformity challenge in membraneless electrolysers without resorting to high-pressure-drop electrode modifications.

2. Design, modelling, and experimentation

2.1. Discharge channel design

Fig. 1(a) shows the elements of a standard membraneless flow-through electrolysis cell schematically. The fluid usually enters the feed channel as a laminar flow, travels sideways through the two perforated electrodes, carrying the produced oxygen and hydrogen bubbles, and then rises and exits through the discharge channels.

Using a highly permeable electrode, as we do, will reduce the overall pressure drop, but will cause fluid to leave the feed channel preferentially near its end. To avoid this, a homogeneous flow through the electrodes can be achieved in at least three ways, schematically depicted in Fig. 1(b)–(d).

First, the electrode's permeability may be tailored to increase in the downstream direction. However, this would present a significant manufacturing challenge and will likely result in substantially increased electrode costs. Second, the feed channel width can be made to decrease in the downstream direction as shown in Fig. 1(c). However, to minimise ohmic losses, the feed channel width should be kept as small as possible everywhere, which results in a non-optimal design. Therefore, we opted for a third option: varying the geometry of the discharge channels. While a straight channel has a simpler cell geometry and can be more compactly distributed over larger areas, the diverging shape shown in Fig. 1(d) can make more effective usage of area when several cells are oriented radially in a circular cross-section stack. It also naturally allows the gas hold-up to increase downstream. A variable discharge channel may add machining complexity and costs. However, if the variable channel proves significantly more efficient, this larger CAPEX could be offset through lower OPEX via higher energy efficiency.

When the flow through the electrodes is homogeneous, the pressure drop over the electrodes is constant, and the pressure gradients in the feed and discharge channels are equal. The discharge channel flow rate will increase linearly with height, which allows its ideal shape to be determined analytically under the Hele-Shaw approximation; see Appendix A for details. The resulting variable width of the discharge channel, $l_d(z)$, as a function of the vertical coordinate z reads

$$l_d(z) = l_f \sqrt[3]{\frac{z}{2h - 2z}} \tag{1}$$

where l_f is the constant width of the feed channel and h is the total height of the electrodes. Fig. 1(b) shows the variable discharge channel shape of Eq. (1).

2.2. Experimental setup and PIV measurements

Fig. 2 shows the experimental setup (a), the used VECO electrodes (b) and an exploded view of the electrolyser (c) of the variable channel width electrolyser. The main body was 3D-printed using a FormLabs 3+ printer with Clear Resin 4.0. Two narrow slots (400 µm wide, 40 mm long) were printed for the electrodes. Two nickel VECO electrodes (ZP200685) with a thickness of 300 µm were inserted and fixed in place using the same resin, maintaining a spacing of 1 mm. Each electrode contains slotted holes (740 µm × 200 µm) with an open area fraction of ϵ =18 % and were inserted into slots to form a l_f = 1 mm inter-electrode

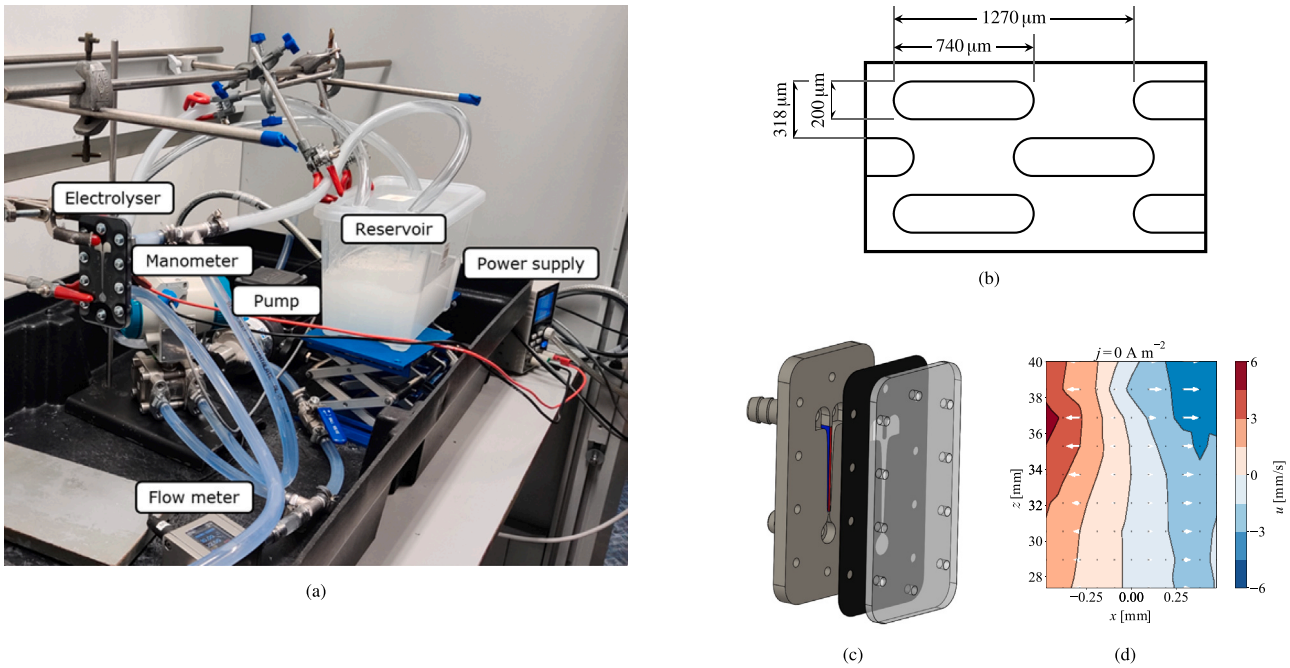


Fig. 2. (a) Overview of the experimental setup. (b) Dimensions of the VECO electrodes (ZP200685) showing the slotted apertures used in the present study. (c) Exploded schematic view of the electrolyser, showing the 3D-printed body (dark grey), EPDM gasket (black), PMMA window (transparent), and electrodes. (d) Contour plot of the horizontal velocity component (u) in the feed channel with no applied current (0 mA cm^{-2}), showing approximately symmetric flow.

gap. With a channel depth of 5 mm, the resulting feed channel cross-section is 5 mm^2, and the electrode length of 40 mm yields an active area of 2 cm^2.

The top of the cell was sealed with a laser-cut 0.5 mm EPDM gasket and a 4 mm thick PMMA face plate, allowing optical access to the inter-electrode region. The assembly is fastened using stainless steel M4 bolts, nuts and washers, as shown in Fig. 2.

From Eq. (1), the discharge channel width diverges as z approaches h. Instead, we cut this off at a height of $z = 0.99$ h. A similar cell was made with a straight discharge channels, whose widths were chosen to be $l_d = 0.5$ mm wide, half that of the feed channel.

A 6 M Potassium Hydroxide (KOH) solution in deionised water is prepared using KOH pellets (≥85 %, Sigma Aldrich). It was circulated through the cell using a Marchmay MK 313 centrifugal magnetic drive pump, to ensure constant flow, without pulsation, this pump is controlled by a TEC E3 Ecodrive variable-frequency drive. The system operated at ambient temperature (22 °C, uncontrolled). The flow rate and temperature are monitored with a MIM-13 01H flow sensor, and the pressure drop across the cell is measured using a Siemens SITRANS P PED-SEP differential pressure transmitter.

The inlet velocity was varied between 0.05 m s^{-1} and 1 m s^{-1}, corresponding to Reynolds numbers in the range of approximately 35–770 within the feed channel. Liquid progressively flows through the electrodes along the channel height. The corresponding average superficial velocity through the electrodes is 0.6 – 13 mm s^{-1}, and the mean velocity inside the electrode holes, dividing by the open-area fraction of $\epsilon = 0.18$, is 3.5 – 69 mm s^{-1}. Experiments were conducted across current densities ranging from open-circuit conditions up to 1 A cm^{-2}.

The electrodes were connected to a DC power supply (Owon SPE6103) using alligator clips. The electrolyser was mounted vertically so that the gas rises along the z-axis.

Flow visualisation within the feed channel was performed using Particle Image Velocimetry (PIV). The electrolyte was seeded with neutrally buoyant polyamide tracer particles of 55 µm diameter. The flow was illuminated with LED panels, and images were captured with a Chronos 1.4 high-speed camera at 1069 frames per second. For each condition, 500 frames were used in an ensemble correlation to obtain statistically converged velocity fields, enabling a direct comparison with the numerical results. Fig. 2(c) shows the region of interest within the feed channel that was investigated, and Fig. 2(d) shows the resulting horizontal velocity field at zero applied current, confirming approximately symmetric flow and thus geometry.

2.3. Numerical model

Model setup. Computational fluid dynamics (CFD) simulations were performed in COMSOL Multiphysics using a multiphase mixture model formulation based on [38]. We modified this model to include two distinct dispersed phases for O_2 and H_2 bubbles. This approach solves a single set of transport equations for the mixture, accounting for the slip velocities between the gas bubbles and the liquid. The model incorporates the key physical phenomena, including buoyancy, hydrodynamic and shear-induced dispersion, and solid pressure. The detailed governing equations and boundary conditions are provided in Appendix B.

Fig. 1(a) schematically shows the two-dimensional simulation domain. The electrode is modelled as a series of discrete channels connecting the feed electrolyte channel to the anode and cathode discharge channels. This two-dimensional representation is derived from the three-dimensional geometry of the Ni-E3 electrode (Veco ZP200685), which contains slotted apertures measuring 740 µm × 200 µm and has an open-area fraction of $\epsilon = 18\%$; see Fig. 2(b). The electrode is represented by a two-dimensional channel with an equivalent hydraulic diameter, $D_h = 4A/P$, where A is the aperture cross-sectional area and P is its wetted perimeter. The spacing between adjacent channels along the electrode is chosen such that the total open area per unit electrode length is preserved, corresponding to the measured open-area fraction of $\epsilon = 18\%$. As in Ref. [38], the fluid dynamics model was coupled with the local current density through the Butler-Volmer equation to account for the electrochemical gas generation at the electrodes. The ionic current density in the electrolyte is governed by Ohm's law, where the bubble-induced reduction in electrolyte conductivity was modelled using the Bruggeman correlation [39]. Boundary conditions included a fully developed laminar parabolic velocity profile at the

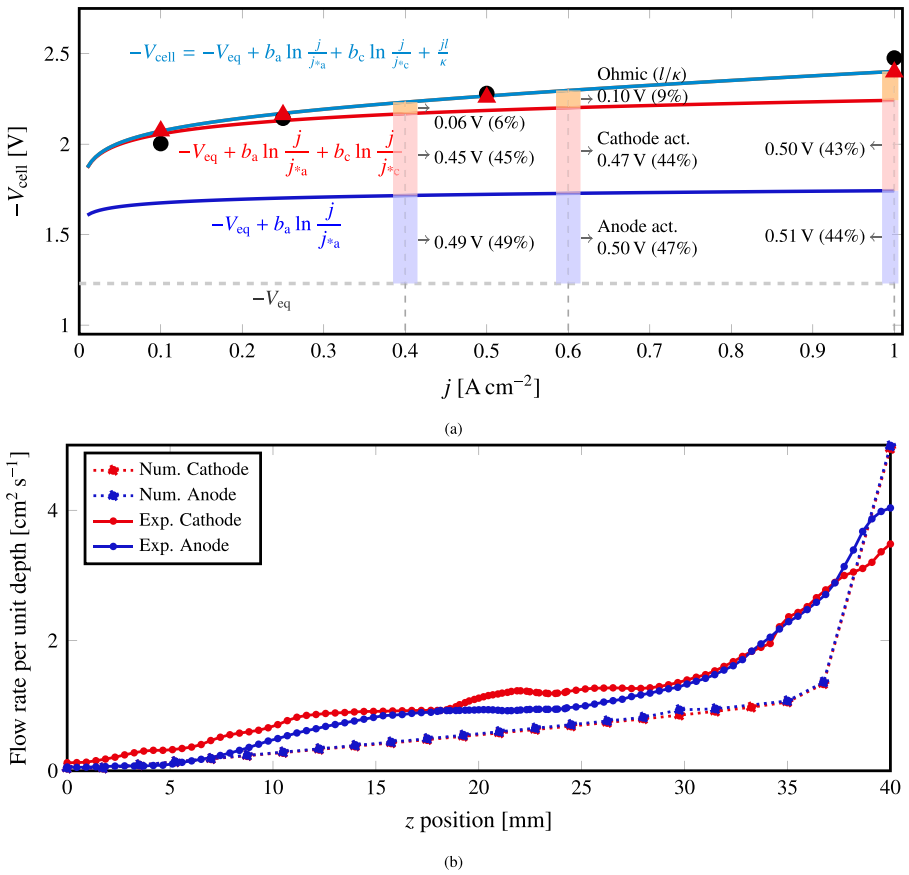


Fig. 3. Validation of the numerical model against experimental data from the variable-width electrolyser prototype. (a) Simulated (▲) and measured (•) cell potentials are shown across a range of current densities. Curves illustrate the cumulative contributions of individual overpotentials: anode activation only (blue), anode + cathode activation (red), and the full cell voltage including electrolyte ohmic resistance (orange). Stacked bands at $j = 400$, 600, and 1 A cm^{-2} decompose the total overpotential into anode activation (blue), cathode activation (red), and electrolyte ohmic loss (orange), with magnitudes and fractions annotated (see text for fitting procedure and contact-resistance estimate). (b) Flow rate per unit depth along the discharge channel height for the anode and cathode sides at $j = 0.05$ A cm^{-2} and a feed inlet velocity of 1.0 m s^{-1}, comparing experimental data against numerical results. (For interpretation of the references to colour in this figure legend, the reader is referred to the web version of this article.)

inlet, a dynamic pressure condition at the outlet, no-slip conditions on the channel walls and electrode surfaces, and a gas flux at the electrode surfaces dictated by Faraday's law of electrolysis. Key simulation parameters are summarised in Table 1.

Mesh refinement study. A mesh refinement study was conducted, using the horizontal velocity component at the anode electrode hole as the convergence criterion. This quantity is particularly relevant because flow through the electrode holes is critical to bubble removal and, hence, to the current density distribution. A mesh with a maximum element size of 60 µm and a minimum element size of 0.2 µm provided approximately grid-independent results. Detailed mesh refinement results are provided in Appendix C.

Model validation. The numerical model was validated against experimental data from a variable-width electrolyser prototype. As shown in Fig. 3(a), the simulated cell potentials agree well with the experimental measurements over a range of current densities. The model slightly differs from the experiment, which may be due to the simulated gas or current distribution, but experimental uncertainty in the feed channel gap width likely also contributes. Fig. 3(a) also provides a simple log-linear formula to describe the data. The ohmic contribution jl/κ uses the feed-channel width l and the bubble-free electrolyte conductivity κ.

The equilibrium potential $-V_{\text{eq}} = 1.23$ V of the water splitting reaction was used. Tafel slopes $b_{\text{a}} = RT/\alpha_{\text{a}}F$ and $b_{\text{c}} = RT/\alpha_{\text{c}}F$ at the anode and cathode, respectively, using data from Ref. [42] obtained for similar electrodes. The exchange current densities $j_{*\text{a}}$ and $j_{*\text{c}}$ were not determined experimentally, but fitted to achieve good agreement. Note

Table 1
Simulation parameters for the alkaline membraneless electrolyser model.

Parameter	Value
Temperature, T	293 K
Liquid density, ρ_{l}	1257 kg m^{-3} [40]
Liquid viscosity, μ_{l}	1.6 mPa s [40]
Hydrogen bubble diameter, d_{b,H_2}	50 µm
Oxygen bubble diameter, d_{b,O_2}	100 µm
Electrolyte conductivity, κ_0	63 S m^{-1} [41]
Anode exchange current density, $j_{*\text{a}}$	0.000 26 A m^{-2}
Cathode exchange current density, $j_{*\text{c}}$	0.62 A m^{-2}
Anode charge transfer coefficient, α_{a}	0.86
Cathode charge transfer coefficient, α_{c}	0.5
Feed channel width, l_{f}	1 mm
Feed channel height, h_{f}	40 mm
Electrode slot dimensions, $w_{\text{s}} \times h_{\text{s}}$	740 µm × 200 µm
Electrode slot hyd. diam., D_{h}	315 µm
Electrode open area fraction, ϵ	0.18

Note: The exchange current densities (j_{a}^*, j_{c}^*) and charge transfer coefficients (α_{a}, α_{c}) are obtained through a combination of experimental data fitting (as shown in Fig. 3(a)) and values from Ref. [42] for similar electrodes. We note that the fit is not unique.

that $b_a \ln(j/j_{*a}) + b_c \ln(j/j_{*c}) = (b_a + b_c)\ln(j/j_*)$, where $j_* \equiv j_{*a}^{1/\alpha_a} j_{*c}^{1/\alpha_c}$. Therefore, the exchange current densities in Table 1 that we used in our simulations are not unique in providing a good fit to the data. Knowing the anode and cathode values individually would require additional reference electrode experiments.

Electrode kinetics are found to dominate at all operating points: at $j = 0.4\,\mathrm{A\,cm^{-2}}$, only 6% is attributable to electrolyte ohmic resistance, with the remaining losses spread roughly equally between anode and cathode activation overpotentials. As the current density increases to $1\,\mathrm{A\,cm^{-2}}$, the ohmic fraction rises to 14%.

Fig. 3(b) compares the experimental and numerical flow rate per unit depth, along the channel height for the anode- and cathode discharge channels in the variable-width discharge channel configuration. The numerical model reproduces the main experimental trends, including the close agreement between flow rate per unit depth in the anode and cathode discharge channels and the pronounced increase in velocity near the channel outlet. Interestingly, the experimental results show that the flow rate is higher in the discharge channels throughout the cell, except at the top holes. This can likely be explained by the clogging of the top holes with gas, increasing the velocities through the holes below the gas cap. This behaviour is not captured in the numerical model.

3. Results and discussion

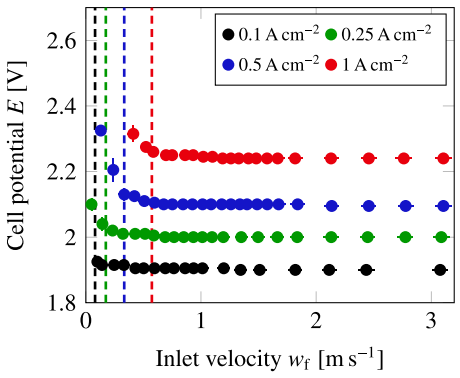
3.1. Critical velocity for stable operation

An important performance metric for membraneless electrolyser operation is the required liquid flowrate at a given current density. The larger the flow rate, the more electrolyte must be pumped, increasing both pumping and gas-separation costs. As argued in Ref. [25], below a critical inlet velocity, bubbles enter the gap and do not leave effectively enough, leading to an additional ohmic drop. There, a maximum additional cell voltage equal to 0.1 V was used to define this critical velocity. Here, it was determined by starting at a high inlet velocity (e.g., $3\,\mathrm{m\,s^{-1}}$) and incrementally decreasing it until a sudden cell potential increase (>2 %) was observed, signalling the onset of gas accumulation as seen in Fig. 4(a).

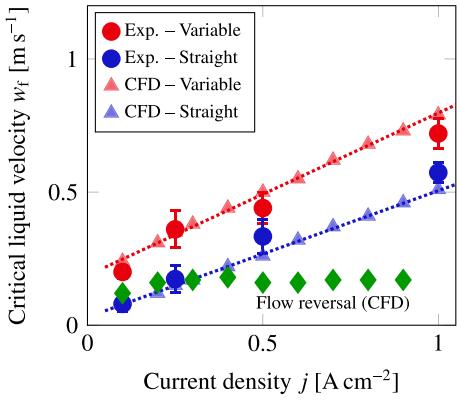
Fig. 4(b) presents the resulting critical liquid velocity (w_f) as a function of current density (j) for both the variable and straight discharge channel configurations. The feed channel is 1 mm wide and 40 mm tall, so to obtain the average flow rate per electrode area, we need to divide the average inlet velocity by 80. From Fig. 4, at $0.4\,\mathrm{A\,cm^{-2}}$ an inlet velocity of about $0.4\,\mathrm{m\,s^{-1}}$ was required, or an average superficial electrode velocity of about $U_l = 5\,\mathrm{mm\,s^{-1}}$, while Ref. [25] needed $3.5\,\mathrm{mm\,s^{-1}}$. This is only slightly lower, but because Nickel felts were used, the hydraulic resistance was much higher.

The critical velocity increases with current density sub-linearly in Refs. [25,44], which was argued to be explainable by capillary action. Here, at least for the straight discharge channel, we find that a linear relation between critical velocity and current density may be more appropriate. A current density of 0.4 A/cm^2 generates roughly $U_g = 0.5$ mm/s of superficial hydrogen flux. Therefore, we find that the average volumetric liquid flux through the electrodes has to be roughly 10 times the gas flux to avoid gas accumulation.

Fig. 5(a)–(c) shows what happens at lower liquid velocities. Since we did not inactive the front of our electrodes, bubbles are also generated inside the gap at all liquid velocities. However, at sufficiently high liquid flow rate, these leave downstream again. Beyond the critical flow rate, the drag forces on the bubbles are insufficient to transport them out of the holes, and instead, bubbles coalesce to form a gas cap at the top of the feed channel. This is what causes the cell voltage to increase beyond the set threshold. Fig. 5(d) and (e) shows how the bubble size increases gradually over the height of the feed channel and time, respectively. After about two seconds, a gap-filling bubble can



(a)



(b)

Fig. 4. (a) Cell potential as a function of liquid inlet velocity at different current densities for the straight discharge channel. Dashed vertical lines mark the critical inlet velocity corresponding to a >2% potential increase. (b) Critical liquid inlet velocity for the onset of gas accumulation as a function of current density. Experimental data (filled circles) indicate the velocity threshold. The CFD predictions based on the criterion that the average gas fraction $\varepsilon_{\mathrm{lasthole}} \approx U_g/\epsilon u_{\mathrm{lasthole}} \leq 0.00735$ (triangles with dotted fit lines) follow an approximately offset-linear dependence on current density. Flow reversal data (diamonds) mark inlet velocities where the horizontal velocity at the anode holes changes direction from outward to inward. (For interpretation of the references to colour in this figure legend, the reader is referred to the web version of this article.)

be seen to arise near the top of the feed channel, only at the highest current density of 0.28 A/cm^2.

Interestingly, the experimental result in Fig. 4 shows that the variable discharge channel, despite providing a more homogeneous flow distribution, consistently requires a higher critical velocity than the straight channel. To understand this observation, we have to look further into the difference in flow profiles between these two cases, which we do in the next section.

3.2. Influence of discharge channel geometry on flow distribution

The modelled velocity profile shown in Fig. 6 shows the same picture as the PIV measurements, but in much more detail and resolution, as well as showing gas fraction. It is clear that the velocity profile through the electrode is far from homogeneous. The liquid inertia causes most of the flow to leave the discharge channel through the last few holes.

Fig. 7 compares the horizontal velocity component (u_{hole}) of the electrolyte as it exits the anode electrode holes for both the straight and variable discharge channel designs. The data is presented for an

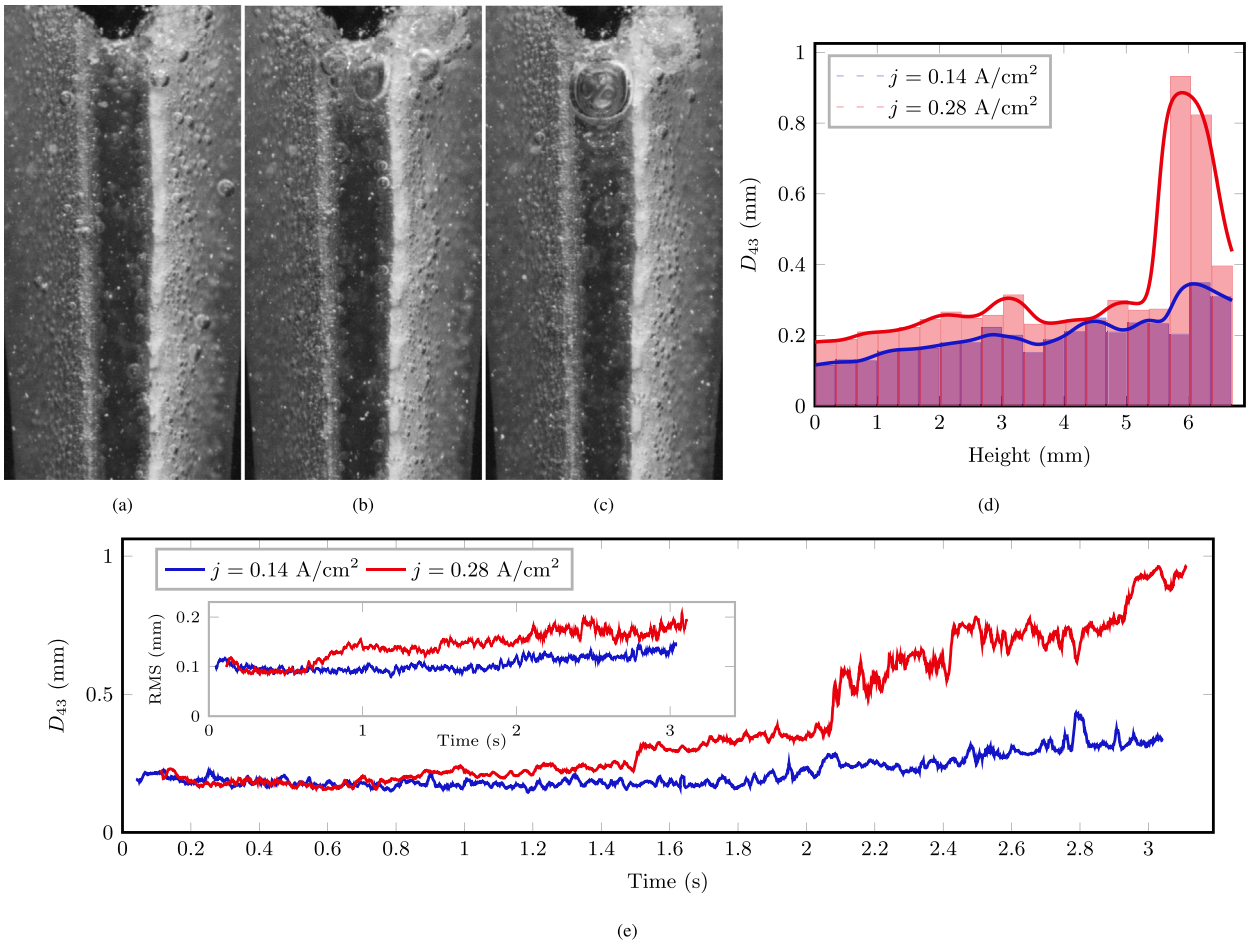


Fig. 5. (a)–(c) Video snapshots of the top of the variable discharge channel geometry; approximately the region highlighted in Fig. 2(c). (a) 1 s, (b) 2 s, (c) 3 s after a current of $j = 0.28$ A/cm^2 is switched on. The feed velocity $w_f = 0.15$ m/s was below the critical velocity, so that a gas cap can be seen to form at the top. The cathode is on the right. See video S1 in the supplementary information for the full video. (d) Volume-weighted bubble diameter $D_{43} \equiv \sum_i D_i^4 / \sum D_i^3$ over all AI-recognised bubbles i using the BubblyFlow script by Küçük et al. [43], in the top ~7 mm of the feed channel for $j = 0.14$ A/cm^2 and $j = 0.28$ A/cm^2 as a function of height, 3 s after switching on the current: bars show 20 bins and the solid lines show the Gaussian kernel estimate with $\sigma = 0.2$ mm. (e) D_{43} over time, smoothed with a 30% noise tolerance; the inset shows the root-mean-square (RMS) diameter $\sqrt{\sum_{i=1}^{N} D_i^2 / N}$ for comparison.

electrolyte inlet velocity of 0.5 m s^{-1} and at three distinct operating current densities: 0.1 A cm^{-2}, 0.4 A cm^{-2}, and 0.8 A cm^{-2}. Compared to the first hole, the velocity decreases by almost an order of magnitude towards the end, then spikes up by two orders of magnitude in the last hole, near the outlet. In contrast, the variable-discharge channel exhibits a much more uniform velocity distribution across most of the electrode holes. This improved distribution confirms that an increasing discharge channel width, as described by Eq. (A.5), can improve flow homogeneity. However, near the end of the channel, and in particular in the last hole, the velocity spikes up strongly. The reason is the inertia of the fluid, which was not included in the simplified analysis of Appendix A.

Because the straight discharge channel is much less wide at the position of the last hole compared to the variable channel, even more electrolyte exists through these last holes. Surprisingly, it seems that because, and not in spite, of this strong inhomogeneity, the straight discharge channel performs well with a lower inlet velocity. The gas cap forming in Fig. 5(a)–(c) can be avoided with a sufficient liquid velocity through the last holes. This can be better appreciated by watching the supplementary videos.

To quantify this assumption, we investigated which parameter in our simulations best correlated with the data on the critical liquid velocity, including the inlet velocity, mean superficial velocity, total pressure drop, gas fraction, centreline velocity, last-hole velocity, and various powers, ratios, and products of these. The best predictor turned out to be the ratio of liquid and gas flowrates through the last hole: the dotted lines in Fig. 4(b) show the condition that the superficial liquid velocity through the topmost hole is 136 times larger than the gas flow rate per unit electrode area. This local criterion works better than any other, more global dimensionless candidates like the Reynolds number, capillary number, or Weber number.

We note that when the superficial liquid velocity ϵu is much larger than the superficial gas velocity U_g and any slip velocity, the gas fraction in the last hole can be approximated by the

$$\epsilon \approx \frac{U_g}{\epsilon u} \tag{2}$$

This immediately follows from ignoring gas fraction variations over the electrode hole area and equating the average liquid velocity u to the gas bubble velocity U_g/ϵ. The criterion $\epsilon u_{\text{lasthole}} > 136 U_g$ can thus be seen to be equivalent to the criterion that the gas fraction in the last hole should stay below approximately 0.7%.

A plausible hypothesis is that above this gas fraction, bubbles can no longer effectively leave through the last hole. Instead, coalescence causes the bubble growth shown in Fig. 5(a)–(c), and leads to the potential increases shown in Fig. 4(a).

This could also explain why the straight discharge channel requires a lower liquid flowrate than the variable discharge channel. Because

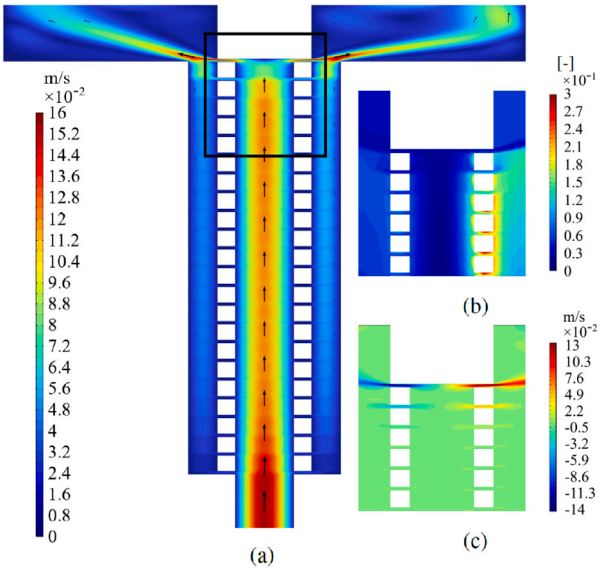


Fig. 6. Straight discharge channel at inlet velocity $0.1\,\mathrm{m\,s^{-1}}$ and current density $0.1\,\mathrm{A\,cm^{-2}}$. White regions represent solid electrode material. (a) Velocity magnitude with superimposed velocity vectors. The solid rectangle marks the zoom region shown in (b) and (c). (b) Gas volume fraction in the zoom region; the cathode side (right) exhibits a higher gas fraction than the anode side (left), consistent with the stoichiometrically larger hydrogen production rate. (c) Horizontal velocity u-component in the zoom region; positive values (red) indicate flow directed towards the cathode discharge channel (right) and negative values (blue) indicate flow towards the anode discharge channel (left), confirming that the electrolyte exits each set of holes towards its respective discharge channel. (For interpretation of the references to colour in this figure legend, the reader is referred to the web version of this article.)

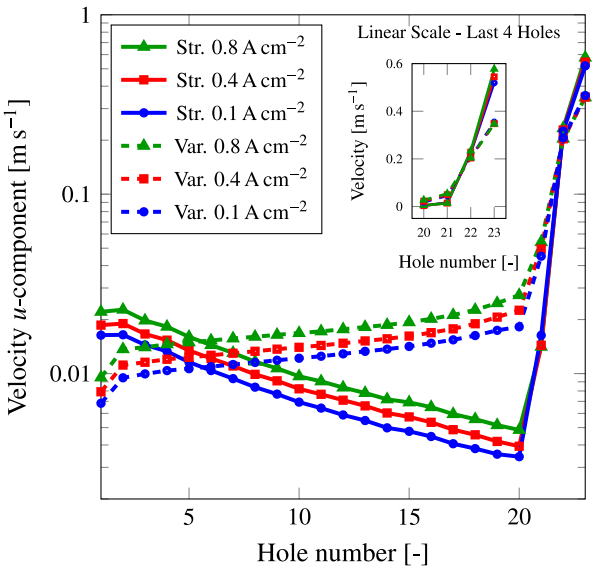


Fig. 7. The horizontal u_{hole}-component velocity at the centre of the anode hole entrances, obtained from numerical simulation. The inlet velocity was $0.5\,\mathrm{m\,s^{-1}}$. The variable-width discharge channel configuration creates a much more homogeneous flow distribution compared to the straight discharge channel. However, its lower flow velocity through the last hole causes more bubbles in the gap. The main plot uses a logarithmic scale, while the zoomed area shows the detailed comparison for the last 4 holes on a linear scale.

its flow is less homogeneous, it has a higher flowrate through the last hole, keeping the gap more effectively free of bubbles.

3.3. Asymmetric buoyancy

We finally turn our attention to a noteworthy prediction of the simulations. Because the gas flux at the hydrogen side is twice that of the oxygen side, a larger buoyancy force is exerted there. The higher upward velocity will draw in more liquid from the feed channel, causing an asymmetry, as shown in Fig. 8. At low liquid flow rates, the flow in the anode can even be seen to reverse as a consequence.

Clearly, this is a very undesirable situation that leads to significant gas crossover. The green diamonds in Fig. 4 show the liquid velocities below which the simulations show flow reversal in the configuration with a variable discharge channel. Luckily, this seems to occur only at liquid flowrates below the critical flowrate, so it does not provide an additional constraint. As a result, we were not able to confirm this hypothesis experimentally, as below the critical liquid velocity, too much gas accumulates. In Fig. 4, at low current densities, the flow reversal curve in Fig. 4 comes close to the critical liquid velocity. Therefore, it will be interesting for future work to investigate the effect experimentally in this regime.

We expect this phenomenon to occur only in the case of very open electrodes, which offer little hydraulic resistance to the asymmetric forcing imposed by buoyancy. If the frictional pressure drop across the electrodes becomes greater, buoyancy will likely have less effect on the flow.

Interestingly, in the simulations, we found no flow reversal in the straight discharge channel configuration, within the investigated range of operating conditions. The reason appears to be that the larger inertia associated with the more inhomogeneous flow in the straight discharge channel is more difficult to reverse by asymmetric buoyancy forces.

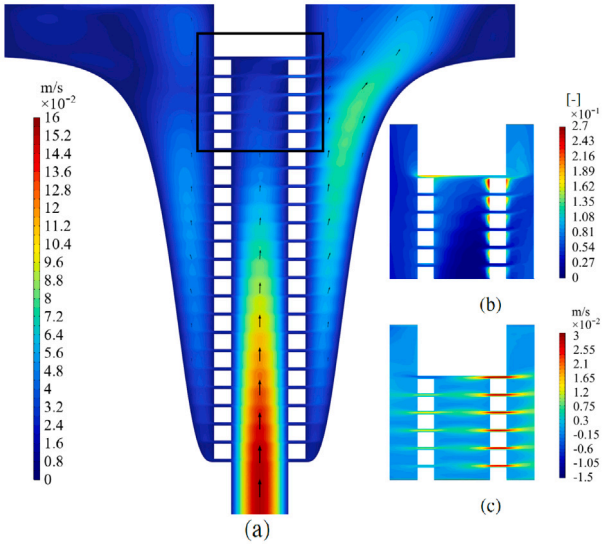


Fig. 8. Variable discharge channel simulations at an inlet velocity $0.1\,\mathrm{m\,s^{-1}}$ and current density $0.1\,\mathrm{A\,cm^{-2}}$, in the regime where flow reversal occurs (see Fig. 4(b)). White regions represent solid electrode material; (a) Velocity magnitude with superimposed velocity vectors. The solid rectangle marks the zoom region shown in (b) and (c). (b) Gas volume fraction in the zoom region; the upper electrode holes show significantly elevated gas accumulation because insufficient liquid flow is available to discharge the gas produced there. (c) Horizontal velocity u-component in the zoom region; on the anode side (left), the holes in the upper region of the electrode (approximately the four holes below the last hole) show positive u-values, indicating that flow is directed towards the cathode rather than towards the anode discharge channel, demonstrating a reversal of the intended flow direction.

4. Conclusions

We studied, both experimentally and computationally, a membraneless alkaline water electrolysis cell with highly permeable electrodes, using a variable-width discharge channel to improve flow uniformity across the electrode holes. Despite its more homogeneous velocity field, higher inlet velocities were required to prevent gas accumulation compared to a straight discharge channel. We found the reason to be the reduced electrolyte velocity through the last holes at the top of the feed channel, which reduces bubble-removal capacity.

On average, the liquid flowrate per unit electrode area has to be about an order of magnitude larger than the hydrogen gas flowrate, similar to what was previously reported for Nickel felts. This makes that the used electrodes will incur significantly smaller pressure drops. However, locally in the top holes, the liquid flowrate must be more than two orders larger than the gas flowrate per unit electrode area. This is equivalent to requiring the gas velocity to stay below about 0.7%. Below this critical liquid velocity, bubbles cannot be effectively removed, and a gas cap was found to appear. We use image recognition to show that bubble coalescence in the inter-electrode gap is responsible. The volume-weighted bubble size was found to increase over the order of seconds and primarily towards the top of the gap.

An interesting additional prediction from the simulations is the onset of flow reversal, driven by the greater buoyancy on the hydrogen side. Luckily, it was simulated to occur only at velocities below the critical liquid velocity and only when the discharge channel widened in the streamwise direction.

These findings highlight that local electrolyte velocities, rather than overall flow uniformity alone, govern the performance of membraneless electrolysers and therefore provide a clear design criterion for future scale-up with highly permeable flow-through electrodes.

CRediT authorship contribution statement

J.I. Postma: Conceptualization, Formal analysis, Investigation, Methodology, Writing – original draft, Writing – review & editing. **A. Yahyaee:** Conceptualization, Formal analysis, Investigation, Methodology, Writing – original draft, Writing – review & editing. **J.W. Haverkort:** Conceptualization, Funding acquisition, Investigation, Supervision, Writing – review & editing.

Funding

This project has received funding from the European Innovation Council (EIC) under grant agreement No 101069981. The EIC receives support from the European Union's Horizon Europe Research and Innovation Programme.

Declaration of competing interest

The authors declare that they have no known competing financial interests or personal relationships that could have appeared to influence the work reported in this paper.

Appendix A. Analytical derivation of discharge channel profile

This appendix repeats, for convenience, the derivation of the discharge channel width profile required to achieve uniform flow distribution through the electrodes previously reported in Ref. [44]. In this case, the pressure gradient over the feed and discharge channel will be identical, denoted by subscripts f and d,

$$\left[\frac{dp}{dz}\right]_{\mathrm{d}} = \left[\frac{dp}{dz}\right]_{\mathrm{f}}. \tag{A.1}$$

With $l_y \gg l$ the electrode thickness in the y-direction, Hele-Shaw flow can be assumed when $w_{\mathrm{d}} l^2/\nu l_y$. Here l is the distance between the walls in the x-direction, either l_{f} or l_{d} in the feed or discharge channel. Furthermore, we assume $h \gg l$. Under these assumptions, the flow will locally approximately satisfy plane Poiseuille flow, and the pressure gradient in the feed and discharge channel can be rewritten to

$$\frac{dp}{dz} = 12\mu\frac{w}{l^2}. \tag{A.2}$$

With μ the dynamic viscosity, w the vertical liquid velocity and substituting Eq. (A.1) into Eq. (A.2), yields

$$\frac{w_{\mathrm{f}}(z)}{l_{\mathrm{f}}^2} = \frac{w_{\mathrm{d}}(z)}{l_{\mathrm{d}}^2}. \tag{A.3}$$

As the velocity decreases linearly over the discharge channel, we can write the feed velocity, w_{f}, as

$$w_{\mathrm{f}}(z) = w_{\mathrm{f}}(0)\left(1 - \frac{z}{h}\right). \tag{A.4}$$

Mass conservation gives the relationship between the feed and discharge velocity as $w_{\mathrm{d}} l_{\mathrm{d}} = \frac{l_{\mathrm{f}}}{2}(w_{\mathrm{f}}(0) - w_{\mathrm{f}}(z))$. Substituting Eq. (A.4), yields $w_{\mathrm{d}}(z) = w_{\mathrm{f}}(0)\frac{z}{h}\frac{l_{\mathrm{f}}}{2l_{\mathrm{d}}}$ and substituting this and Eq. (A.4) into Eq. (A.3), we find

$$l_{\mathrm{d}}(z) = l_{\mathrm{f}}\sqrt[3]{\frac{z}{2h - 2z}}. \tag{A.5}$$

Reversing the argument, we find that under the given assumptions and with the discharge channel satisfying Eq. (A.5), the flow velocity through the electrode will be homogeneously distributed.

Appendix B. Numerical model: Governing equations and boundary conditions

We use gas volume fractions $\varepsilon_{\mathrm{O_2}}$ for oxygen and $\varepsilon_{\mathrm{H_2}}$ for hydrogen, with the total gas fraction defined as $\varepsilon = \varepsilon_{\mathrm{O_2}} + \varepsilon_{\mathrm{H_2}}$. The mixture's volume-averaged velocity is:

$$\mathbf{U} = (1-\varepsilon)\mathbf{u}_{\mathrm{l}} + \varepsilon_{\mathrm{O_2}}\mathbf{u}_{\mathrm{O_2}} + \varepsilon_{\mathrm{H_2}}\mathbf{u}_{\mathrm{H_2}}, \tag{B.1}$$

where $\mathbf{u}_{\mathrm{l}}$, $\mathbf{u}_{\mathrm{O_2}}$, and $\mathbf{u}_{\mathrm{H_2}}$ represent the velocities of the liquid, oxygen, and hydrogen phases, respectively. With gas densities negligible compared to the liquid density ρ_{l}, the mixture density is:

$$\rho_{\mathrm{m}} = (1-\varepsilon)\rho_{\mathrm{l}}. \tag{B.2}$$

The mass-averaged mixture velocity $\mathbf{U}_{\mathrm{m}}$ matches the superficial liquid velocity:

$$\mathbf{U}_{\mathrm{m}} = \mathbf{U}_{\mathrm{l}} = (1-\varepsilon)\mathbf{u}_{\mathrm{l}}. \tag{B.3}$$

The steady-state mixture continuity equation is:

$$\nabla \cdot \mathbf{U}_{\mathrm{m}} = 0. \tag{B.4}$$

A single momentum equation describes the transport of the three-phase mixture:

$$\rho_{\mathrm{m}}(\mathbf{u}_{\mathrm{l}} \cdot \nabla)\mathbf{u}_{\mathrm{l}} = -\nabla p + \nabla \cdot \mathbf{K} - \rho_{\mathrm{m}}\mathrm{g}\hat{\mathbf{z}}, \tag{B.5}$$

where the mixture viscosity is $\mu_{\mathrm{m}} = \mu_{\mathrm{l}}/(1-\varepsilon)$ [45], and the viscous stress tensor is $\mathbf{K} = \mu_{\mathrm{m}}\left(\nabla\mathbf{U} + (\nabla\mathbf{U})^{\mathrm{T}}\right)$.

The velocities of the oxygen and hydrogen phases are characterised by slip velocities: $\mathbf{u}_{s,\mathrm{O_2}} = \mathbf{u}_{\mathrm{O_2}} - \mathbf{u}_{\mathrm{l}}$ and $\mathbf{u}_{s,\mathrm{H_2}} = \mathbf{u}_{\mathrm{H_2}} - \mathbf{u}_{\mathrm{l}}$. The slip fluxes are:

$$\mathbf{U}_{s,\mathrm{O_2}} = \varepsilon_{\mathrm{O_2}}(1-\varepsilon)\mathbf{u}_{s,\mathrm{O_2}}, \quad \mathbf{U}_{s,\mathrm{H_2}} = \varepsilon_{\mathrm{H_2}}(1-\varepsilon)\mathbf{u}_{s,\mathrm{H_2}}. \tag{B.6}$$

From the continuity of each gas phase, we derive:

$$\mathbf{U} \cdot \nabla\varepsilon_{\mathrm{O_2}} + \nabla \cdot \mathbf{U}_{s,\mathrm{O_2}} = 0, \tag{B.7}$$

$$\mathbf{U} \cdot \nabla\varepsilon_{\mathrm{H_2}} + \nabla \cdot \mathbf{U}_{s,\mathrm{H_2}} = 0. \tag{B.8}$$

Each slip velocity is composed of four contributing mechanisms:

$$\mathbf{u}_{s,i} = \mathbf{u}_{\mathrm{St},i} + \mathbf{u}_{\mathrm{Hd},i} + \mathbf{u}_{\mathrm{Sd},i} + \mathbf{u}_{\mathrm{Sp},i}, \tag{B.9}$$

where $i = O_2$ or H_2, representing Stokes' buoyancy-driven rise, hydrodynamic dispersion, shear-induced diffusion, and solid pressure effects, respectively.

Adapting formulations from prior work [46], these mechanisms assume force balance, with Stokes' drag valid for bubbles under 100 µm [47]:

Stokes' rise velocity (buoyancy-driven vertical motion):

$$\mathbf{u}_{\mathrm{St},i} = f(\varepsilon) w_{\mathrm{St},i} \hat{\mathbf{z}}, \tag{B.10}$$

where $w_{\mathrm{St},i} = \rho_\mathrm{l} g d_{\mathrm{b},i}^2/(18\mu_\mathrm{l})$ is the terminal velocity due to buoyancy, and $d_{\mathrm{b},i}$ is the bubble diameter for each gas.

Hydrodynamic dispersion:

$$\mathbf{u}_{\mathrm{Hd},i} = -f(\varepsilon)\frac{d_{\mathrm{b},i} w_{\mathrm{St},i}}{2}\frac{\nabla \varepsilon_i}{\varepsilon_i}, \tag{B.11}$$

Shear-induced diffusion:

$$\mathbf{u}_{\mathrm{Sd},i} = -\frac{d_{\mathrm{b},i}^2}{4}\left|\frac{\partial v}{\partial x} + \frac{\partial u}{\partial y}\right| \frac{\varepsilon_i(1 + 0.5\mathrm{e}^{8.8\varepsilon})}{3(1-\varepsilon)} \nabla \varepsilon_i, \tag{B.12}$$

The hindrance function $f(\varepsilon) = (1-\varepsilon)^4$ accounts for reduced bubble mobility at high gas fractions [48,49].

Solid pressure term (dispersion at high gas fractions) [38]:

$$\mathbf{u}_{\mathrm{Sp},i} = -\frac{d_{\mathrm{b},i}^2 \nabla p_{\mathrm{s},i}}{18\mu_\mathrm{l}\varepsilon_i}, \tag{B.13}$$

with the solid pressure gradient given by:

$$\nabla p_{\mathrm{s},i} = \gamma_0 \rho_\mathrm{l} g d_{\mathrm{b},i} \nabla\left(\frac{(\varepsilon_i - \varepsilon_{\min})^{\gamma_1}}{(\varepsilon_{\max} - \varepsilon_i)^{\gamma_2}}\right), \tag{B.14}$$

using $\gamma_0 = 0.002$, $\gamma_1 = 2$, $\gamma_2 = 5$, $\varepsilon_{\min} = 0$, and $\varepsilon_{\max} = 0.65$ [50], consistent with experimental data [51].

The liquid phase comprises a concentrated potassium hydroxide (KOH) solution, enabling oxygen and hydrogen evolution at the anode and cathode:

$$\text{Cathode:} \qquad 4H_2O + 4e^- \rightarrow 4OH^- + 2H_2, \tag{B.15}$$

$$\text{Anode:} \qquad 4OH^- \rightarrow 2H_2O + O_2 + 4e^-. \tag{B.16}$$

Hydroxide ions act as charge carriers, balanced by K^+ for electroneutrality [39]. Under high KOH concentration and sufficient mixing, the electrolyte is treated as uniform, with ionic current density governed by Ohm's law:

$$\mathbf{i} = -\kappa \nabla \phi, \tag{B.17}$$

where κ is the effective conductivity and ϕ is the electric potential. Gas bubbles reduce the effective conductivity, approximated using Bruggeman's model [39]:

$$\kappa = \kappa_0 (1-\varepsilon)^{3/2}, \tag{B.18}$$

where κ_0 is the intrinsic conductivity of the bubble-free electrolyte.

Electrode reaction kinetics follow the Butler-Volmer relation:

$$j_\perp = j^*\left(\mathrm{e}^{\frac{\alpha \mathrm{F}\eta}{\mathrm{RT}}} - \mathrm{e}^{-\frac{(1-\alpha)\mathrm{F}\eta}{\mathrm{RT}}}\right), \tag{B.19}$$

where $j_\perp$ is the local current density normal to the electrode surface, j^* is the exchange current density, α is the charge transfer coefficient, F is the Faraday constant, R is the universal gas constant, T is temperature, and $\eta = (E-\phi) - (E-\phi)_{\mathrm{eq}}$ is the overpotential [39].

Boundary conditions

At the inlet, a fully developed flow condition is applied by specifying an average velocity:

$$U_{\mathrm{av}} = \frac{1}{\hat{A}}\int_{\Omega_{\mathrm{inl}}} \mathbf{u}\cdot\mathbf{n}\,\mathrm{d}S, \tag{B.20}$$

where $\hat{A}$ is the inlet cross-sectional area, Ω_{inl} is the inlet boundary, and $\mathbf{n}$ is the outward unit normal vector.

Table C.2
Mesh refinement scenarios evaluated in the convergence study.

Scenario	Max element size [µm]	Min element size [µm]
1	200	5
2	100	2
3	60	0.2
4	50	0.18

At the outlet, a dynamic pressure boundary condition is imposed:

$$(-p\mathbf{I} + \mathbf{K})\cdot\mathbf{n} = -p_{\mathrm{out}}\mathbf{n}, \tag{B.21}$$

where the outlet pressure is defined as

$$p_{\mathrm{out}} = -\rho_\mathrm{l} g \mathrm{H} + \begin{cases} -\frac{1}{2}\rho_\mathrm{l}\left(w(x)(1-\varepsilon)\right)^2, & w(x) < 0, \\ 0, & w(x) \geq 0, \end{cases} \tag{B.22}$$

with ρ_l the liquid density, g the gravitational acceleration, H the vertical distance between the inlet and the outlet, $w(x)$ the vertical velocity component, ε the local gas volume fraction, $\mathbf{n}$ the outward unit normal vector, $\mathbf{I}$ is the identity tensor, and $\mathbf{K}$ is the viscous stress tensor.

Symmetry conditions are applied at the outer computational boundaries, ensuring no flow across the boundary and zero tangential stress:

$$\mathbf{U}\cdot\mathbf{n} = 0, \quad \mathbf{t}^{\mathrm{T}}\mathbf{K}\mathbf{n} = 0, \tag{B.23}$$

where $\mathbf{t}$ is the tangent vector.

A no-slip condition is enforced at the discharge channel walls:

$$\mathbf{U} = 0. \tag{B.24}$$

At the electrode surfaces, the gas flux and mixture velocity are determined by the electrochemical gas production rates according to Faraday's law:

$$\varepsilon_i \mathbf{u}_i = \mathbf{U} = -U_i \mathbf{n}, \tag{B.25}$$

where $U_i = \mathcal{V}_{\mathrm{m}} j_\perp/(n_i F)$, with $\mathcal{V}_{\mathrm{m}}$ being the molar volume of gas at standard conditions, $n_{\mathrm{H}_2} = 2$ for hydrogen, and $n_{\mathrm{O}_2} = 4$ for oxygen.

The anode potential is fixed at a reference value:

$$E_\mathrm{a} = 0. \tag{B.26}$$

At the cathode, the average current density is enforced:

$$\frac{1}{S_\mathrm{e}}\int_{S_\mathrm{e}} j_\perp\,\mathrm{d}S_\mathrm{e} = j, \tag{B.27}$$

where S_e is the electrode surface and j is the specified applied current density.

Appendix C. Mesh refinement study

Four progressively refined mesh configurations were evaluated, with maximum element sizes ranging from 200 µm to 50 µm and minimum element sizes from 5 µm to 0.18 µm. The mesh refinement parameters are summarised in Table C.2.

The horizontal velocity component in each of the anode holes for the straight and variable discharge channel configurations, evaluated at an input velocity of 0.5 m s^{-1} and a current density of 0.1 A cm^{-2} is provided in Figure S7. The results demonstrate clear convergence behaviour as the mesh is refined, with scenarios 3–4 producing virtually identical results across all hole positions. Based on this analysis, scenario 3 with a maximum element size of 60 µm and a minimum element size of 0.2 µm was selected for all subsequent simulations. The negligible difference between scenarios 3–4 confirms that further refinement would not yield meaningful improvements in the solution quality.

Appendix D. Supplementary data

Supplementary videos and figures are provided to support the results discussed in this paper. S1 and S2 are at 140 mA cm^{-2} and 280 mA cm^{-2} respectively at an inlet velocity of 0.15 m/s. S3 to S6 show the flow behaviour in the top and bottom sections of both the variable and straight discharge channel configurations at 50 mA cm^{-2} at an inlet velocity of 1 m/s. The white particles seen in the video are the PIV tracer particles.

Supplementary material related to this article can be found online at https://doi.org/10.1016/j.ecmx.2026.102272.

Data availability

Data will be made available on request.

References

[1] David M, Ocampo-Martínez C, Sánchez-Peña R. Advances in alkaline water electrolyzers: A review. J Energy Storage 2019;23:392–403. http://dx.doi.org/10.1016/j.est.2019.03.001.

[2] Phillips R, Dunnill C. Zero gap alkaline electrolysis cell design for renewable energy storage as hydrogen gas. RSC Adv 2016;6:100643–51. http://dx.doi.org/10.1039/C6RA22242K.

[3] Haug P, Koj M, Turek T. Influence of process conditions on gas purity in alkaline water electrolysis. Int J Hydrog Energy 2017;42:9406–18. http://dx.doi.org/10.1016/j.ijhydene.2016.12.111, URL: https://www.sciencedirect.com/science/article/pii/S0360319916336588.

[4] Groot MT De, Kraakman J, Barros RLG. Optimal operating parameters for advanced alkaline water electrolysis. Int J Hydrog Energy 2022;47:34773–83.

[5] Niblett D, Delpisheh M, Ramakrishnan S, Mamlouk M. Review of next generation hydrogen production from offshore wind using water electrolysis. J Power Sources 2024;592:233904.

[6] Aili D, Kraglund MR, Rajappan SC, Serhiichuk D, Xia Y, Deimede V, Kallitsis J, Bae C, Jannasch P, Henkensmeier D, Jensen JO. Electrode separators for the next-generation alkaline water electrolyzers.

[7] de Groot MT, Vreman AW. Ohmic resistance in zero gap alkaline electrolysis with a zirfon diaphragm. Electrochim Acta 2021;369:137684. http://dx.doi.org/10.1016/j.electacta.2020.137684.

[8] Haverkort JW, Rajaei H. Voltage losses in zero-gap alkaline water electrolysis. J Power Sources 2021;497:229864. http://dx.doi.org/10.1016/j.jpowsour.2021.229864.

[9] Raman A, van der Werf S, Eyövge C, Olguin MA Rodriguez, Schlautmann S, Rivas D Fernández, Mei B, Gardeniers H, Susarrey-Arce A. A zero-gap silicon membrane with defined pore size and porosity for alkaline electrolysis. Sustain Energy Fuels 2024;8:3296–303. http://dx.doi.org/10.1039/D4SE00515E.

[10] Esposito D. Membraneless electrolyzers for low-cost hydrogen production in a renewable energy future. Joule 2017;1:651–8. http://dx.doi.org/10.1016/j.joule.2017.07.003.

[11] Haverkort J, Rajaei H. Electro-osmotic flow and the limiting current in alkaline water electrolysis. J Power Sources Adv 2020;6:100034.

[12] Lohmann R, Cousins IT, DeWitt JC, Glüge J, Goldenman G, Herzke D, Lindstrom AB, Miller MF, Ng CA, Patton S, Scheringer M, Trier X, Wang Z. Are fluoropolymers really of low concern for human and environmental health and separate from other PFAS?. Environ Sci Technol 2020;54:12820–8. http://dx.doi.org/10.1021/acsenergylett.3c00185; ACS Energy Letters 2023;8:1900–10;

[13] von Tettau P, Thiele P, Mauermann P, Wick M, Tinz S, Pischinger S. Per- and polyfluoroalkyl substances in proton exchange membrane fuel cells — a review J Power Sources 2025;630:236104.

[14] Manzotti A, Robson MJ, Ciucci F. Recent developments in membraneless electrolysis Curr Opin Green Sustain Chem 2023;40:100765. http://dx.doi.org/10.1016/j.cogsc.2023.100765.

[15] Perskaya R, Zaidenman I. On liquid diffusion electrodes In: Doklady akademii nauk. vol. 115, Russian Academy of Sciences; 1957, p. 548–51.

[16] Sioda R. Distribution of potential in a porous electrode under conditions of flow electrolysis Electrochim Acta 1971;16:1569–76.

[17] Pletcher D, Hampson NA, McNeil AJS. The electrochemistry of porous electrodes: Flow-through and three-phase electrodes In: Pletcher D, editor. Electrochemistry. vol. 9, Royal Society of Chemistry; 1984, p. 1–65. http://dx.doi.org/10.1039/9781847559944-00001.

[18] Kinoshita K, Leach S. Mass-transfer study of carbon felt, flow-through electrode J Electrochem Soc 1982;129:1993.

[19] Wang J, Dewald H. Deposition of metals at a flow-through reticulated vitreous carbon electrode coupled with on-line monitoring of the effluent J Electrochem Soc 1983;130:1814.

[20] El-Anadouli B, Khader M, Saleh M, Ateya B. Application of porous flow through electrodes: Iv. hydrogen evolution on packed bed electrodes of iron spheres in flowing alkaline solutions J Appl Electrochem 1991;21:166–9.

[21] Saleh MM. Simulation of oxygen evolution reaction at porous anode from flowing electrolytes J Solid State Electrochem 2007;11:811–20.

[22] Ateya B, Arafat E. Applications of porous flow-through electrodes: I. an experimental study on the hydrogen evolution reaction on packed bed electrodes J Electrochem Soc 1983;130:380.

[23] Gillespie M, Kriek R. Scalable hydrogen production from a mono-circular filter press divergent electrode-flow-through alkaline electrolysis stack J Power Sources 2018;397:204–13. http://dx.doi.org/10.1016/j.jpowsour.2018.07.026.

[24] Gillespie M, van der Merwe F, Kriek R. Performance evaluation of a membraneless divergent electrode-flow-through (deft) alkaline electrolyser based on optimisation of electrolytic flow and electrode gap J Power Sources 2015;293:228–35. http://dx.doi.org/10.1016/j.jpowsour.2015.05.077, URL: https://www.sciencedirect.com/science/article/pii/S0378775315009684.

[25] Rajaei H, Rajora A, Haverkort J. Design of membraneless gas-evolving flow-through porous electrodes J Power Sources 2021;491:229364. http://dx.doi.org/10.1016/j.jpowsour.2020.229364.

[26] Niblett D, Elwan HA, Mamlouk M. Membraneless water electrolysis enabled by flow and porous electrode design for bubble separation Chem Eng J 2025;519:163444. http://dx.doi.org/10.1016/j.cej.2025.163444, URL: https://www.sciencedirect.com/science/article/pii/S1385894725042780.

[27] Davis JT, Qi J, Fan X, Bui JC, Esposito DV. Floating membraneless pv-electrolyzer based on buoyancy-driven product separation Int J Hydrog Energy 2018;43:1224–38.

[28] O'Neil GD, Christian CD, Brown DE, Esposito DV. Hydrogen production with a simple and scalable membraneless electrolyzer J Electrochem Soc 2016;163:F3012–9. http://dx.doi.org/10.1149/2.0021611jes.

[29] Davis JT, Brown DE, Pang X, Esposito DV. High speed video investigation of bubble dynamics and current density distributions in membraneless electrolyzers J Electrochem Soc 2019;166:F312–21. http://dx.doi.org/10.1149/2.0961904jes.

[30] Gillespie M, Kriek R. Hydrogen production from a rectangular horizontal filter press divergent electrode-flow-through (deft™) alkaline electrolysis stack J Power Sources 2017;372:252–9.

[31] Kriek RJ, van Heerden LA, Falch A, Gillespie MI, Faid AY, Seland F. On the electrocatalytic symbiotic synergism between pt, ni and al in plasma vapour deposited ptxniyalz thin metal films for water electrolysis J Power Sources 2021;494:229344.

[32] Schoppmann K, Rox H, Frense E, Rüdiger F, Yang X, Eckert K, Fröhlich J. Why shape matters: Hydrodynamics of a y-shaped membraneless electrolyzer Chem Eng J 2025;507:160040.

[33] Marini S, Salvi P, Nelli P, Pesenti R, Villa M, Berrettoni M, Zangari G, Kiros Y. Advanced alkaline water electrolysis Electrochim Acta 2012;82:384–91. http://dx.doi.org/10.1016/j.electacta.2012.05.011.

[34] Zeng K, Zhang D. Recent progress in alkaline water electrolysis for hydrogen production and applications Prog Energy Combust Sci 2010;36:307–26. http://dx.doi.org/10.1016/j.pecs.2009.11.002.

[35] Swiegers GF, Terrett RNL, Tsekouras G, Tsuzuki T, Paceb RJ, Strange R. The prospects of developing a highly energy-efficient water electrolyser by eliminating or mitigating bubble effects Sustain Energy Fuels 2021;5:1280. http://dx.doi.org/10.1039/D0SE01886D.

[36] Angulo A, van der Linde P, Gardeniers H, Modestino M, Rivas DF. Influence of bubbles on the energy conversion efficiency of electrochemical reactors Joule 2020;4:555–79.

[37] Zhang L, Iwata R, Lu Z, Wang X, Díaz-Marín CD, Zhong Y. Bridging innovations of phase change heat transfer to electrochemical gas evolution reactions Chem Rev 2024;124:10052–111.

[38] van der Does WL, Valle N, Haverkort JW. Multiphase alkaline water electrolysis simulations: The need for a solid pressure model to explain experimental bubble overpotentials Int J Hydrog Energy 2025;102:295–303. http://dx.doi.org/10.1016/j.ijhydene.2024.12.252.

[39] Haverkort JW. Electrolysers, fuel cells and batteries. TU Delft OPEN Publishing; 2024.

[40] Kuznetsov KI, Skorodumov SV, Granchenko PP. Measurements of the dynamic viscosity and density of koh solutions at atmospheric pressure High Temp 2020;58:806–11. http://dx.doi.org/10.1134/S0018151X20060127.

[41] Gilliam R, Graydon J, Kirk D, Thorpe S. A review of specific conductivities of potassium hydroxide solutions for various concentrations and temperatures Int J Hydrog Energy 2007;32:359–64. http://dx.doi.org/10.1016/j.ijhydene.2006.10.062, URL: https://www.sciencedirect.com/science/article/pii/S0360319906005428, fuel Cells.

[42] Haverkort JW, Aghdam AS, Craye EJB. The optimal electrode hole size in zero gap alkaline water electrolysis: A combined electrochemical, theoretical, and bubble imaging approach Int J Hydrog Energy 2025;171:150919.

[43] Küçük S, Della Santina C, Laskari A. Segmenting the complex and irregular in two-phase flows: A real-world empirical study with SAM2 Int J Multiph Flow 2026;196:105557. http://dx.doi.org/10.1016/j.ijmultiphaseflow.2025.105557.

[44] Deiters GB. Minimizing bubble losses in membraneless flow-through water electrolysis [Master's thesis], Delft University of technology; 2023, Available at https://resolver.tudelft.nl/uuid:20d051dd-390f-49b4-b043-782346f6a89b.

[45] Ishii M, Zuber N. Drag coefficient and relative velocity in bubbly, droplet or particulate flows AIChE J 1979;25:843–55. http://dx.doi.org/10.1002/aic.690250513.
[46] Dahlkild AA. Modelling the two-phase flow and current distribution along a vertical gas-evolving electrode J Fluid Mech 2001;428:249–72. http://dx.doi.org/10.1017/S0022112000002639.
[47] Clift R, Grace JR, Weber ME. Bubbles, drops, and particles. Courier Corporation; 2005.
[48] Schillings J, Doche O, Deseure J. Modeling of electrochemically generated bubbly flow under buoyancy-driven and forced convection Int J Heat Mass Transfer 2015;85:292–9. http://dx.doi.org/10.1016/j.ijheatmasstransfer.2015.01.121.
[49] Rajora A, Haverkort JW. An analytical multiphase flow model for parallel plate electrolyzers Chem Eng Sci 2022;260. http://dx.doi.org/10.1016/J.CES.2022.117823.
[50] Johnson PC, Nott P, Jackson R. Frictional-collisional equations of motion for particulate flows and their application to chutes J Fluid Mech 1990;210:501–35. http://dx.doi.org/10.1017/S0022112090001380.
[51] Coenen EL, Janssen LJ. Voidage of bulk solution in a tall vertical gas evolving cell J Appl Electrochem 1997;27:1143–8. http://dx.doi.org/10.1023/A:1018411331833.